Meta Distribution of the SIR in a Narrow-Beam LEO Uplink

Ilari Angervuori, *Student Member, IEEE* , Martin Haenggi, *Fellow, IEEE*, and Risto Wichman, *Senior Member, IEEE*

***Abstract*—We focus on stochastic geometry analysis of a low Earth orbit (LEO) narrowband terrestrial-satellite uplink with satellite base stations (SBSs) in a uniform constellation equipped with narrow Gaussian beams. The served and interfering omnidirectional user equipments (UEs) are distributed on the Earth's surface according to a homogeneous Poisson point process (HPPP) with Nakagami faded signals. This study presents a detailed but comprehensive mathematical analysis of several key metrics: the signal-to-interference ratio (SIR), the SIR meta distribution (MD), the signal-to-interference-plus-noise ratio (SINR), and the average throughput. Many results are presented in simple analytical and closed forms containing more insight than the expressions proposed in prior works. The results indicate an optimal UE density depending on the altitude, elevation angle, and the width of the antenna gain, maximizing the average throughput. However, this optimal density leads to a significant variance in the user experience regarding link quality (*i.e.*, the users are not treated fairly).**

***Index Terms*—Low Earth orbit, stochastic geometry, coverage probability, meta distribution, average throughput, Lomax distribution.**

I. Introduction

A. Motivation

Fifth-generation (5G) and beyond wireless communication systems are setting new standards of reliability and connectivity [1]. The emerging Low Earth Orbit (LEO) satellite networks have the potential to significantly increase coverage, especially in far-flung areas: incorporating such networks with terrestrial networks can facilitate a seamless coverage continuum [2]. Several large LEO constellation projects are already being developed and planned, including Starlink, Kuiper, LeoSat, OneWeb, and Telesat. Kuiper, LeoSat, OneWeb, and Telesat. 3GPP aims to adapt existing satellite and terrestrial networks to provide direct connectivity from hand-held equipment to LEO satellites using frequencies assigned to mobile satellite services or those assigned to legacy terrestrial networks. An extensive study of potential LEO network configurations is presented in [3], indicating that numerous implementations are possible. Due to the large footprint, a single satellite can serve several user equipments (UEs). At the same time, the large cell size causes interference between terrestrial and non-terrestrial users and systems.

The *Vilho, Yrjö and Kalle Väisälä Foundation* supported this work by making the research visit and collaboration with the University of Notre Dame possible.

I. Angervuori is with the Department of Electrical Engineering, Aalto University, Espoo, 02150, Finland. (email: ilari.angervuori@aalto.fi)

M. Haenggi is with the Department of Electrical Engineering, University of Notre Dame, Notre Dame, IN 46556, USA. (email: mhaenggi@nd.edu)

R. Wichman is with the Department of Electrical Engineering, Aalto University, Espoo, 02150, Finland. (email: risto.wichman@aalto.fi).

The stochastic geometry system-level analysis offers valuable insights that complement other link and system-level models and simulations of terrestrial and non-terrestrial communications. This analytical method helps us understand how different deployment parameters affect performance metrics. In particular, it provides comprehensive information on the satellite base station (SBS) reliability, coverage probability, and throughput. Ultimately, this knowledge aids in determining optimal network configurations and allows for more efficient allocation of simulation resources.

B. Related work

As a relatively new concept introduced in [4], the analysis of the signal-to-interference ratio (SIR) meta distributions (MD) for terrestrial networks has become well-established in the literature. Additionally, SIR MD has been applied to the LEO networks. An analysis of the SIR MD under the Nakagami fading model was proposed in [5] and [6], where the SIR MD was studied in a LEO downlink. Both papers model the satellites by either the homogeneous Poisson point process (HPPP) or the homogeneous binomial point process (HBPP) on a sphere and the transmitters as a HPPP, allowing the ergodic interpretation of the SIR MD as "what fraction of users can achieve a given transmission reliability for a given SIR threshold". [1] In [5], the satellites were assumed to have an omnidirectional antenna beam. In contrast, in [6], a perfect beam alignment with the terrestrial base station was assumed, causing no interference to the other devices. To the best of our knowledge, the SIR MDs for the LEO uplink are yet to be explored.

The following literature review focuses on papers on the proposed state-of-the-art stochastic geometry frameworks in the LEO uplink. A comprehensive literature review addressing other LEO scenarios can be found in [8]. Furthermore, the book [9] has been published on the subject. The work in [10] is one of the first papers addressing the stochastic geometry modeling of the LEO uplink, where the coverage probability and average throughput were studied assuming omnidirectional antennas for both the satellite and the transmitters. As in many similar works, the PPP model for the satellites has proven effective in approximating deterministic constellations. In [11], the SIR distribution was studied for large network densities in an interference-only channel with a Gaussian antenna beam under Rician fading with a two-tier shadowing model. A

[1] Although strictly speaking, the HPPP is not ergodic on the sphere, the condition for the ergodicity [7, Def. 2.30] holds approximately for large densities.

TABLE I: Stochastic geometry LEO uplink and LEO SIR MD models in the literature

Proposed by	**Scenario**	**Earth transmitter model**	**Satellite constellation model**	**Earth-to-satellite fading and shadowing model**	**System metrics and results** in C=closed-form expression A=analytic expression M=mathematical expression	**System type**	**Satellite antenna model**
This paper	Uplink direct communication	HPPP	Uniform constellation	Nakagami fading	SIR MD (M for the moments), Coverage probability (A), Average throughput (C)	Interference-limited, Interference-plus-noise-limited	Narrow Gaussian beam
[5]	Downlink direct communication	HPPP	HPPP	Nakagami fading	SIR MD (A for the moments)	Interference-limited	Omni-directional
[6]	Downlink hybrid network	HPPP	HBPP	Nakagami fading	SIR MD (A for the moments)	Interference-limited	Perfect beam alignment
[10]	Uplink direct communication	HPPP	HPPP	Shifted exponential power fading	Coverage probability (M), Average throughput (M)	Interference-limited	Omni-directional
[11]	Uplink direct communication	HPPP	Uniform constellation	Rician fading with a two-tier shadowing model	Coverage probability (A)	Interference-limited	Narrow Gaussian beam
[12]	Uplink direct communication	HPPP	HPPP, Walker-Star,	Shadowed Rician fading	Coverage probability (M), Average throughput (M)	Interference-plus-noise-limited	ITU-R beam
[13]	Uplink direct communication	HPPP	Deterministic polar constellation	Shadowed Rician fading	Coverage probability (M), Average throughput (M)	Interference-plus-noise-limited	ITU-R beam
[14]	Uplink direct communication	HBPP	HBPP, Walker-Star, Walker-Delta	Gaussian mixture shadowing model	Coverage probability (M)	Interference-plus-noise-limited	Boxcar function
[15]	Uplink hybrid communication	HPPP	HPPP, Walker-Star, Walker-Delta	Gaussian mixture shadowing model	Coverage probability (M)	Interference-plus-noise-limited	Boxcar function
[16]	Uplink direct and hybrid communication	Poisson cluster process	HBPP	Shadowed Rician fading	Coverage probability (M)	Interference-plus-noise-limited	Boxcar function
[17]	Uplink direct communication	HPPP, Poisson hard-core p.p.	Deterministic two altitude circular orbits	Rician fading	Coverage probability (A)	Interference-plus-noise-limited	Perfect beam alignment and constant sidelobes

shadowed Rician model and a realistic ITU-R antenna beam were used in [12] and [13]. Similar to this paper, in [12], it was noted that a particular constellation density maximizes the throughput. The system model is realistic; however, the derived formulas are complicated to evaluate and may lack clear insight. A Gaussian mixture model for the fading with a boxcar-type antenna beam model was used in [14] and [15]. Modeling was based on working with the mean interference from the transmitters, which may be accurate with wide antenna beams; however, the mean fails to grasp the highly varying nature of the interference in narrow antennas. Uplink hybrid and direct communication with IoT devices, including battery lifetime, were studied in [16]. Similar to this paper and [12], in [16], an optimal density for the satellites (proportional to the number of Earth transmitters) was found to maximize the performance. Similar to this paper, a planar HPPP model was used in [17]. Additionally, in [17], the Poisson hard-core model was introduced. All of the mentioned papers and the system model details are summarized in Table I.

We present a tractable analytical framework for the narrow-beam LEO that yields insightful results distinct from previous works. Additionally, our paper offers a fine-grained analysis of the variation in the uplink quality of the SBSs, which has yet to be addressed in the existing literature.

C. *Our contributions*

The contributions of the work are listed as follows.

- We present a novel, simplified, narrow-beam LEO system model that provides a tractable analytical framework for stochastic geometry analysis.
- We derive the moments of the SIR MD and study user experiences in different network settings through the distribution.
- We derive the SIR distribution in a closed form and the signal-to-interference-plus-noise ratio (SINR) distribution in analytic form.
- We derive the average throughput in a simple closed form and an optimal density for the Poisson layout of UEs that maximizes the average rate.
- We observe a significant trade-off between the optimal average throughput and user experience consistency regarding the link quality.

D. *Organization of the paper*

In Section II, we formulate and compare the planar and spherical system models and introduce the fading and antenna pattern models. Section III derives the moments of the SIR MD and provides two different approximations based on the moments: beta distribution and Chebyshev-Markov inequalities. In Section IV, we study the SIR, SINR, and throughput distributions. The key insights of the results are summarized in Section V.

II. System model

We present two system models: the simplified planar system model used in the analysis and the spherical system model used in the simulations. A sketch of the simplified planar system model is depicted in Figures 1a and 1b.

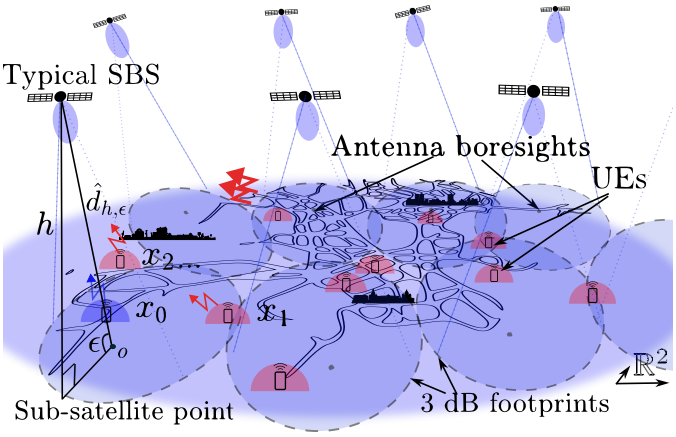

(a) Interpretation of the *planar* system model with the SBSs in adjacent orbits serving an urban area and a realization of the UEs. The altitudes are not to scale.

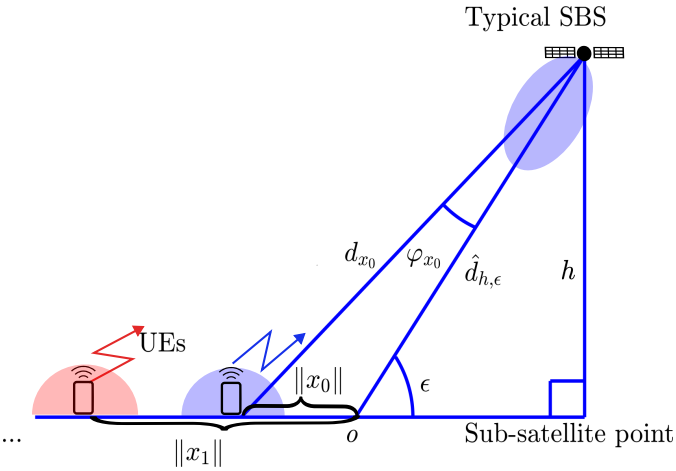

(b) The typical SBS as seen from the side. The transmitters are projected into line $(0, \infty)$ according to their norm.

Fig. 1: The simplified narrow-beam LEO uplink system model. The SBS antenna boresight is oriented towards o, the focus point of the elliptical footprint. The omnidirectionally transmitting UEs $\{x_i\}$ are located according to the HPPP on the plane. The nearest transmitter, x_0, is the served UE.

TABLE II: Glossary of principal symbols

Symbol	Explanation
h	Altitude of the SBSs.
ϵ	Elevation angle of the SBSs.
$G[\cdot]$	The SBS antenna gain.
φ_{RX}	Halfwidth of the SBSs -3 dB gain.
$\Theta \subset E$	HPPP on the Earth surface $E \subset \mathbb{R}^3$ of density λ.
$\Phi \subset \mathbb{R}^2$	HPPP on the plane of density λ.
$\|x\|$	Distance of $x \in \Phi$ from the origin $o = (0,0) \in \mathbb{R}^2$.
x_0	Nearest point to the origin in Φ.
$D_{h,\epsilon}$	A scaling constant of $\|x\|$; $D_{h,\epsilon} = \sin^2(\epsilon)/h$.
κ	Parameter that reflects the approximate mean number of UEs inside a SBS -3 dB footprint; $\kappa = \lambda\pi(h\varphi_{\text{RX}}/\sin^2(\epsilon))^2$.
$\tilde{\kappa}$	$\kappa/\log(2)$.
m	Nakagami-m fading parameter.
g_x	The power fading gain of mean 1 of a transmitter $x \in \Phi$ or $x \in \Theta$. Corresponds to a Nakagami-m distributed amplitude fading; $m = 1$ corresponds to the exponential distribution, and $m = \infty$ is deterministic.
θ	SIR or SINR threshold for a successful transmission.
I	Interference at the typical SBS in the planar model.
S	The signal power of the served UE at the typical SBS in the planar model.
$\mathring{I}$	Interference at the typical SBS in the spherical model.
$\mathring{S}$	The signal power of the served UE at the typical SBS in the spherical model.
$\hat{d}_{h,\epsilon}/d_0$	The distance between the SBS and the focus point in the planar model divided by a normalizing distance.
W	Constant noise power.
γ	Power path loss exponent.

A. *Approximate planar model of the narrow-beam LEO uplink*

We study a short period of use over multiple coherence times in a high-frequency narrow-band terrestrial-satellite uplink Nakagami fast-fading channel in a single-tier network. The link quality from the perspective of a SBS is investigated. We assume that UEs with omnidirectional antennas, like mobile phones, are randomly located on the Earth surface, represented as a plane. The SBSs can work as an independent network or complement a terrestrial network, and the interfering transmitters can be considered to be within the same cell, adjacent cells, overlapping cells, or part of a terrestrial network served by a terrestrial BS.

The UEs form a HPPP $\Phi \subset \mathbb{R}^2$ of density λ. The Poisson assumption can be justified by the independent mobility patterns of UEs. Furthermore, the multipath fading of the signals can make an arbitrary network seem Poisson at the receiver [18, Sec. 4.3]. The SBSs form a homogeneous point pattern (deterministic or random), allowing the ergodic interpretation of the performance metrics over the SBSs. Because the HPPP is translation invariant, all points are statistically equivalent. Therefore, we can refer to the concept of a *typical* SBS. The SBS antennas are narrow-beam considered to serve a local homogeneous environment, such as a rural or urban area. Consequently, the scattering and attenuation caused by the weather conditions and Doppler shifts are the same for all relevant UEs, thus not affecting their relative signal strengths at the SBS.

We study the SIR and SINR distributions at the typical SBS serving the terrestrial UE from which it receives the maximum mean signal power. The UEs are transmitting at the normalized power $P = 1$. The typical SBS is at altitude h, and its Gaussian antenna's $G[\cdot]$ gain boresight is directed toward a point on the Earth surface for which the SBS is at the elevation angle ϵ—this is a focus point of the elliptical footprint, considered the origin $o \triangleq (0,0) \in \mathbb{R}^2$. The values of h and ϵ determine the distance to the satellite from o, given by the geometric relation $\hat{d}_{h,\epsilon} \triangleq h/\sin(\epsilon)$. In this work, we focus on LEO altitudes of $h \in [200, 2000]$ km. We will consider that $\epsilon \geq 45°$. (We restrict the elevation angle to ensure the simplified narrow-beam LEO model is accurate. However, we make an exception in Figures 3a, 3b and 4, where we compare the spherical and the planar models with the elevation angle $\epsilon = 35°$, which is the minimum elevation angle in a LEO system proposed in [19].)

This work focuses on the SIR and SINR of the nearest transmitter. The served UE is formally defined as

$$x_0 \triangleq \arg\min\{x \in \Phi : \|x\|\}, \tag{1}$$

where $\|\cdot\|$ is the Euclidean distance.

In the following, we write $f(x) \sim g(x)$, as $x \to a$, if the limit $\lim_{x\to a} f(x)/g(x) = 1$. Considering Figure 1b, for each angle φ_x between the transmitter $x \in \Phi$ and the typical SBS antenna boresight, we have

$$\varphi_x \sim D_{h,\epsilon}\|x\|, \ \|x\| \to 0, \tag{2}$$

where $D_{h,\epsilon} \triangleq \sin^2(\epsilon)/h$ is the derivative of the function $\|x\| \mapsto \varphi_x$ at $\|x\| = 0$ (the details given in Appendix A). Note that (2) is only the first-order Taylor expansion of φ_x at $\|x\| = 0$; the approximation is sufficient if the antenna pattern decays fast for large φ_x.

Let us define the path loss law by

$$\ell(x) \triangleq \frac{G[\varphi_x]}{(d_x/d_0)^\gamma}, \quad \gamma \geq 0, \tag{3}$$

where d_x is the distance between the UE and the SBS, and d_0 is a normalizing distance. Combining (2) with (3) yields $\ell(x) \sim G[D_{h,\epsilon}\|x\|]/(d_x/d_0)^\gamma, \ \|x\| \to 0$.

Furthermore, we assume a narrow antenna beam and the relevant transmitters are located in a small region close to each other around o and $d_x \approx \hat{d}_{h,\epsilon}$ for the relevant $x \in \Phi$. Along these lines, the random process of path losses $\{x \in \Phi : \ell(x)\}$ is approximated with the gain process (GP)

$$\mathcal{G} = \{x \in \Phi : G[D_{h,\epsilon}\|x\|]\} \tag{4}$$

multiplied by the constant $(\hat{d}_{h,\epsilon}/d_0)^{-\gamma}$.

$\mathcal{G}$ is a particular case of the projection process that has been extensively studied in the literature [18, Ch. 4]. By the mapping theorem [7, Thm. 2.34], it is a PPP on $(0, 1)$. [2]

Because of its analytical tractability, we model the small-scale fading with the Nakagami-m fading model, where $m \in \mathbb{N}$ is the Nakagami fading parameter. For each UE $x \in \Phi$, the amplitude fading gain follows an independent Nakagami distribution with shape parameter m and spread parameter 1. Hence, each transmission power is multiplied by an independent gamma-distributed fading gain g_x of mean 1 with shape and scale parameters m and $1/m$, respectively. The Nakagami distribution closely approximates the Rician distribution, widely utilized as a fading model in satellite communications [20, Sec. 6.7.1]. Furthermore, the gamma distributed power fading can be used to approximate the shadowed Rician power fading distribution [16].

The antenna gain $G[\cdot] : [0, \infty) \to (0, 1]$ is assumed to be Gaussian, *i.e.*,

$$G[\varphi] = 2^{-\varphi^2/\varphi_{\text{RX}}^2}, \tag{5}$$

where φ_{RX} is the halfwidth of the -3 dB antenna gain. Except Section II-C, we use the value $\varphi_{\text{RX}} = 1.6°$, corresponding to the LEO antenna pattern proposed in the International Telecommunication Union Recommendations (ITU-R) [21]. Despite being an idealized antenna pattern, the Gaussian response accurately models the main lobe (-10 dB lobe) of many antenna patterns, particularly the ITU-R pattern, cf. Figure 2. This work considers the interference energy from the sidelobes a nonnegative constant noise but is not explicitly characterized. This approach works as long as the UE density is high enough and the served UE is likely to be in the main lobe. [3]

[2]Interestingly, incorporating independent fading r.v.'s $\{H_x\}$ the projection process with the fading $\{x \in \Psi : H_x G[D_{h,\epsilon}\|x\|]\}$ can appear Poisson, even if the underlying Ψ is not a PPP [18, Sec. 4.3].

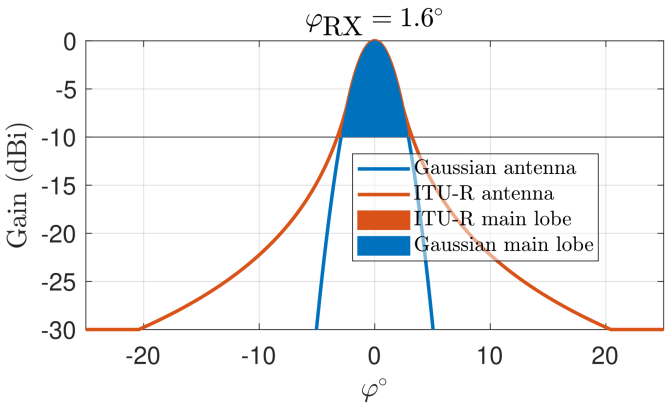

Fig. 2: Comparison between the Gaussian and [21, ITU-R LEO reference radiation patterns]. The gain of the Gaussian antenna in the main lobe (-10 dB lobe) is almost identical to the ITU-R main lobe. However, there is a slight difference towards the edges of the main lobe. The fast-decaying Gaussian beam essentially corresponds to the main lobe component.

B. *Spherical system model and Monte Carlo simulation*

A sketch of the geometry of the spherical model is presented in Appendix B.

We compare the analytical results from the planar model to Monte Carlo simulations of the spherical model. The Monte Carlo simulations assume a spherical Earth with a radius of $R_\oplus = 6378$ km. We denote the HPPP of the UEs visible to the satellite of density λ on the Earth surface by $\Theta \subset E$. The number of samples depends on the density: we simulate, on average, 10^6 UEs inside the -100 dB footprint (of the Gaussian beam). The elliptical footprint's antenna boresight location is the ellipse's nearest focus point, o_E—the ellipse represented in terms of latitude and longitude. The PPP on the sphere can be constructed from the PPP on the plane by the *area-preserving* mapping $(x_1, x_2) \mapsto (1, x_1, \sin^{-1}(x_2))$ from the rectangle $[-\pi, \pi] \times [-1, 1]$ to the spherical coordinates. We use a homography from the ellipse to a circle to find the SBS antenna gain of each UE. In the Monte Carlo simulations, the angles $\{\varphi_u\}$, the distances $\{d_u\}$, $u \in \Theta$, and consequently the path loss law (3) are based on the spherical Earth model and calculated by basic geometry. For example, we have

$$d_{h,\epsilon} \triangleq d_{o_E} = \sqrt{R_\oplus^2 + (R_\oplus + h)^2 - 2R_\oplus(R_\oplus + h)\cos(\xi)} \tag{6}$$

for the distance between the SBS and the focus point o_E, where $\xi = \xi(\epsilon)$ is the central angle between o_E and the sub-satellite point on the spherical Earth's surface (the details given in Appendix B). The fading model is the Nakagami-m, and the antenna gain is Gaussian (5).

[3]Analogously to the semi-analytical simulation methods [22], the possible interference component from the sidelobes can be modeled with a constant corresponding to the mean aggregate power from the interferers outside the main lobe because of the relatively small variance of the total interference. Hence, the sidelobe component can be incorporated in a constant noise term.

C. *Total received power and its convergence properties in the planar model w.r.t. the spherical model*

In this section, we compare the *total received power* from all transmitters in the system model presented in Section II with that of the spherical model in Section II-B.

We define $u_0 \triangleq \arg\min\{u \in \Theta : d_u\}$. The total received power at the typical SBS from the UEs in the PPP Θ on the Earth's surface above the horizon is defined as

$$\mathring{P}_{\text{tot}} \triangleq \mathring{I} + \mathring{S} = \sum_{u\in\Theta} g_u \ell(u) = \sum_{u\in\Theta} \frac{g_u G[\varphi_u]}{(d_u/d_0)^\gamma}, \tag{7}$$

where $\mathring{S}$ is the signal strength at the receiver of the nearest transmitter u_0, and $\mathring{I}$ is the interference component consisting of the received signal powers from $\Theta \setminus \{u_0\}$.

We validate the approximate system model by studying the convergence properties of the mean and the second moment of the simulated $\mathring{P}_{\text{tot}}$ to the mean and the second moment of

$$P_{\text{tot}} \triangleq I + S = \frac{\sum\limits_{x\in\Phi} g_x G[D_{h,\epsilon}\|x\|]}{(\hat{d}_{h,\epsilon}/d_0)^\gamma} = \frac{\sum\limits_{x'\in\mathcal{G}} g_x x'}{(\hat{d}_{h,\epsilon}/d_0)^\gamma}. \tag{8}$$

The fading models are equal in the planar and spherical models, and the difference is in the geometry. Hence, we focus on the geometric accuracy of the approximate model and set $g_x \equiv 1$, *i.e.*, $m = \infty$, in this subsection. The fading does not affect the first moment of the total received power. In the following, we refer to Lemma 1 regarding the density $\lambda_{\mathcal{G}}(r) = \tilde{\kappa}/r$, $\tilde{\kappa} = \lambda\pi\left(h\varphi_{\text{RX}}/\sin^2(\epsilon)\right)^2/\log(2)$, and the Poisson property of the GP (which is needed for the variance). For $g_x \equiv 1$, [7, Cor. 4.8] gives the expected value and the variance, $\text{var}(P_{\text{tot}}) = \mathbb{E}(P_{\text{tot}}^2) - \mathbb{E}(P_{\text{tot}})^2$, of P_{tot}:

$$\begin{aligned}\mathbb{E}(P_{\text{tot}}) &= \left(\frac{d_0}{\hat{d}_{h,\epsilon}}\right)^\gamma \int_{\mathbb{R}^2} G[D_{h,\epsilon}\|x\|]\lambda dx \\ &= \left(\frac{d_0}{\hat{d}_{h,\epsilon}}\right)^\gamma \int_0^1 r\lambda_{\mathcal{G}}(r)dr = \frac{d_0^\gamma h^{2-\gamma}\pi\lambda\varphi_{\text{RX}}^2}{\sin^{4-\gamma}(\epsilon)\log(2)}, \end{aligned} \tag{9}$$

$$\begin{aligned}\text{var}(P_{\text{tot}}) &= \left(\frac{d_0}{\hat{d}_{h,\epsilon}}\right)^{2\gamma} \int_{\mathbb{R}^2} G[D_{h,\epsilon}\|x\|]^2\lambda dx \\ &= \left(\frac{d_0}{\hat{d}_{h,\epsilon}}\right)^{2\gamma} \int_0^1 r^2\lambda_{\mathcal{G}}(r)dr = \frac{d_0^\gamma \sin^\gamma(\epsilon)}{2h^\gamma}\mathbb{E}(P_{\text{tot}}). \end{aligned} \tag{10}$$

An interesting observation from (9) and (10) is that for the free-space path loss exponent $\gamma = 2$, for given λ, ϵ, and φ_{RX}, the mean of the total received power does not depend on the altitude of the typical SBS; the path loss becomes increasingly prominent, but there are more UEs present in the main lobe as we increase h. However, $\text{var}(P_{\text{tot}})$ rapidly increases when we decrease the altitude. On the other hand, P_{tot} approaches a constant for large h. For $\gamma > 2$, the expected total received power decreases as the altitude increases. For $\gamma = 4$, $\mathbb{E}(P_{\text{tot}})$ does not depend on the elevation angle of the SBS.

Figures 3a and 3b show the total received powers $\mathring{P}_{\text{tot}}$ and P_{tot} for $\gamma \in \{2, 4\}$ for different ϵ and h. The insights derived from the theoretical model of mean and variance apply to the spherical model, especially for $\gamma = 2$. For $\gamma = 2$, the average total received power is approximately independent of the altitude, and for $\gamma = 4$, the received power is almost independent of the elevation angle.

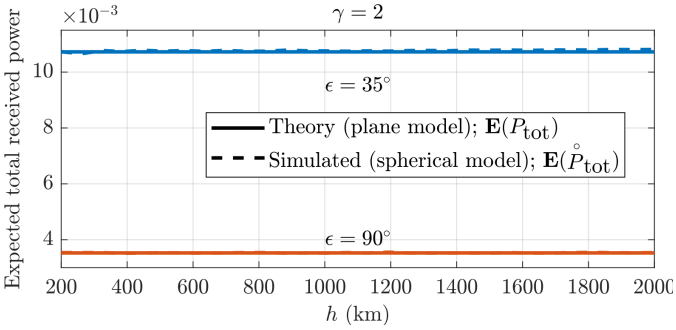

(a) The average total received power for the path loss exponent $\gamma = 2$ as a function of altitude h.

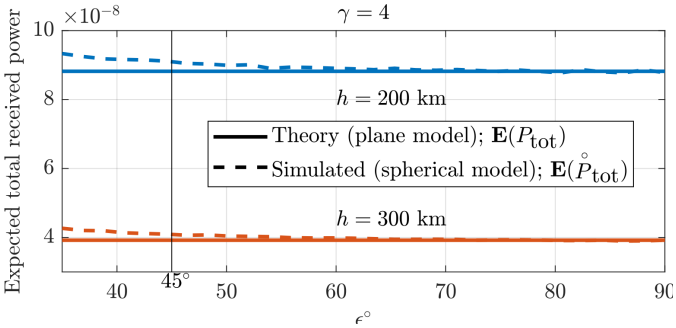

(b) The average total received power for the path loss exponent $\gamma = 4$ as a function of elevation angle ϵ.

Fig. 3: Comparison of the expected total received power based on the simulated spherical model and the theoretical planar model. The parameters $\varphi_{\text{RX}} = 1.6°, P = 1, \lambda = 1/\text{km}^2, \gamma \in \{2, 4\}, h \in [200, 2000]$ km, $\epsilon \in [35°, 90°]$ are used.

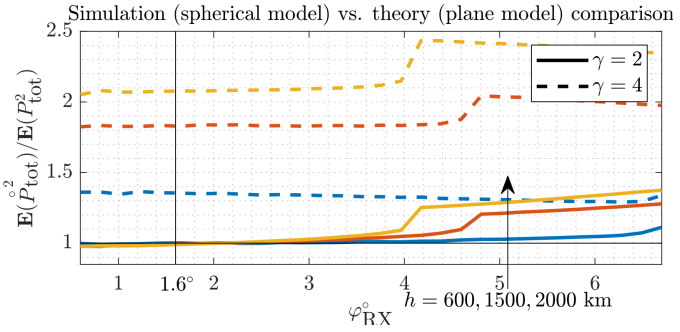

Fig. 4: The ratio of the second moments of the simulated and theoretical total received powers. The parameters $h \in \{600, 1500, 2000\}$ km, $\lambda = 1/\text{km}^2, \epsilon = 35°, \varphi_{\text{RX}} \in [0.6°, 6.7°]$ and $\gamma \in \{2, 4\}$ are used.

Figure 4 shows the ratio of the second moments $\mathbb{E}(\mathring{P}_{\text{tot}}^2)/\mathbb{E}(P_{\text{tot}}^2)$ w.r.t. the antenna width $\varphi_{\text{RX}} \in [0.6°, 6.7°]$ for different values of h and γ. The density $\lambda = 1/\text{km}^2$, and the elevation angle $\epsilon = 35°$, which is the minimum elevation angle in a LEO system proposed in [19]. Due to the geometry, it is the worst-case scenario for the error between the models. The ratios for $\epsilon > 35°$ are closer to 1 for each h. The ratios tend to 1 for $\gamma = 2$ as $\varphi_{\text{RX}} \to 0$. There is a threshold after which $\mathbb{E}(\mathring{P}_{\text{tot}}^2)$ becomes exponentially larger than $\mathbb{E}(P_{\text{tot}}^2)$. This is caused by the differences in the geometry. However, the horizon restricting the energy from the UEs in the spherical model limits this exponential increase for larger

φ_{RX}. For $\gamma = 4$, convergence to 1 does not happen. This is due to the difference in the averages of $\{d_u\}_{u\in\Theta}$ and $\{d_x\}_{x\in\Phi}$, which cancels out for $\gamma = 2$. The theoretical model could be improved using the more complicated $d_{h,\epsilon}$ instead of $\hat{d}_{h,\epsilon}$ in (8). However, the theoretical SIR is independent of the path loss exponent, which also holds (up to the accuracy we are interested in) in the spherical model. We will validate this using the path loss exponents $\gamma \in \{2, 4\}$ in the simulations in Sections III and IV.

Similar but faster convergence to 1 was observed for the first moments $\mathbb{E}(\mathring{P}_{\text{tot}})/\mathbb{E}(P_{\text{tot}})$ than for $\mathbb{E}(\mathring{P}^2_{\text{tot}})/\mathbb{E}(P^2_{\text{tot}})$.

Based on these observations, we put forth that, for $\gamma = 2$ or $\epsilon = \pi/2$, $\mathbb{E}(P_{\text{tot}}) \sim \mathbb{E}(\hat{P}_{\text{tot}})$ and $\mathbb{E}(P^2_{\text{tot}}) \sim \mathbb{E}(\hat{P}^2_{\text{tot}})$ as $\varphi_{\text{RX}} \to 0$. Furthermore, it is natural to conjecture that the convergence holds for any moment and thus for the distribution. Hence, in distribution, $\mathring{P}_{\text{tot}} \approx P_{\text{tot}}$ for the narrow beams. We will demonstrate that similar convergence also applies to the SIR and SINR.

D. *Relative Gain Process*

The analysis of Sections III and IV is based on the following formulation of the relative gain process.

DEFINITION 1 (Relative gain process (RGP)). Let $\Phi \subset \mathbb{R}^2$ be a HPPP. The relative gain process is defined as

$$\mathcal{G} \triangleq \left\{ x \in \Phi \setminus \{x_0\} : \frac{G[D_{h,\epsilon}\|x\|]}{G[D_{h,\epsilon}\|x_0\|]} \right\}. \tag{11}$$

The following lemma gives the density function of the RGP. The equivalence GP=RGP is a useful implication of the lemma, with the GP defined in (4).

LEMMA 1. The GP and the RGP are inhomogeneous PPPs on $(0, 1) \ni r$ with the density function

$$\lambda_{\mathcal{G}}(r) = \tilde{\kappa}/r, \tag{12}$$

where $\tilde{\kappa} = \kappa/\log(2)$ and

$$\kappa \triangleq \lambda\pi \left(\frac{h\varphi_{\text{RX}}}{\sin^2(\epsilon)} \right)^2 \tag{13}$$

is approximately the mean number of UEs inside a SBS -3 dB footprint.

Proof. The process $\{x \in \Phi : \|x\|^2\}$ is Poisson distributed on $(0, \infty)$ with the density $2\pi\lambda$ [7, Example 2.9]. Consequently, the distances $\|x_k\|^2 - \|x_0\|^2$ in $G[D_{h,\epsilon}\|x_k\|]/G[D_{h,\epsilon}\|x_0\|] = 2^{-(\|x_k\|^2 - \|x_0\|^2)/\varphi^2_{\text{RX}}}$ between the kth nearest point and the nearest point are Erlang distributed with parameters $k \geq 1$ and $2\pi\lambda$ regardless of x_0. Hence, without loss of generality, we can condition $x_0 = o$. Furthermore, by Slivnyak's theorem, $\{x \in \Phi \setminus \{x_0\} : \|x\|^2 - \|x_0\|^2\}$ reduces to the process $\{x \in \Phi : \|x\|^2\}$ for $x_0 = o$, and the result follows by applying the mapping theorem [7, Thm. 2.34] to the GP;

$$\int_r^1 \lambda_{\mathcal{G}}(y)dy = \lambda\pi \left(\frac{G^{-1}[r]}{D_{h,\epsilon}} \right)^2 = \lambda\pi \left(\frac{h\varphi_{\text{RX}}\sqrt{-\log(r)}}{\sin^2(\epsilon)\sqrt{\log(2)}} \right)^2$$

for $0 < r < 1$. $G^{-1}[\cdot]$ is the inverse function of $G[\cdot]$. $\lambda_{\mathcal{G}}(r)$ follows by derivation w.r.t. r and taking the minus sign.

The interpretation of κ as the mean number of UEs inside the -3 dB footprint follows by solving $D_{h,\epsilon}\|x_{\text{RX}}\| = \varphi_{\text{RX}}$ for the distance $\|x_{\text{RX}}\|$ to the edge of the -3 dB footprint and from the area formula of a circle and Campbell's theorem. In line with (2), this interpretation of κ is exact in the limit $\varphi_{\text{RX}} \to 0$. □

For any measurable function $v(\cdot) : \mathbb{R}^d \to [0, 1]$ such that $\int_{\mathbb{R}^d} |\log v(x)|\lambda_\Psi(x)dx < \infty$, the probability-generating functional (PGFL) $\mathfrak{G}_\Psi(\cdot)$ of a point process (p.p.) Ψ is defined by

$$\mathfrak{G}_\Psi[v] \triangleq \mathbb{E} \prod_{x\in\Psi} v(x). \tag{14}$$

We use Lemma 1 to derive the PGFL of the RGP [18, Eq. (3.30)];

$$\begin{aligned} \mathfrak{G}_{\mathcal{G}}[v] &= \exp\left\{ -\int_{\mathbb{R}} (1 - v(r))\lambda_{\mathcal{G}}(r)dr \right\} \\ &= \exp\left\{ -\tilde{\kappa}\int_0^1 (1 - v(r))/rdr \right\}. \end{aligned} \tag{15}$$

E. *The signal-to-interference ratio*

The SIR at the typical SBS can be represented in terms of the GP. It is defined as

$$\begin{aligned} \text{SIR}_{\kappa,m} &\triangleq \frac{S}{I} = \left(\frac{I}{S}\right)^{-1} \\ &= \left(\frac{\sum\limits_{x\in\Phi\setminus\{x_0\}} Pg_x G[D_{h,\epsilon}\|x\|]/(\hat{d}_{h,\epsilon}/d_0)^\gamma}{Pg_{x_0} G[D_{h,\epsilon}\|x_0\|]/(\hat{d}_{h,\epsilon}/d_0)^\gamma} \right)^{-1} \\ &= g_{x_0}/\sum_{x'\in\mathcal{G}} g_x x', \end{aligned} \tag{16}$$

where $x' = G[D_{h,\epsilon}\|x\|]/G[D_{h,\epsilon}\|x_0\|]$ and $\{g_x\}_{x\in\Phi}$ are i.i.d. Gamma distributed r.v.'s. We represent the SIR in terms of the interference-to-signal ratio (ISR) in order to represent the SIR in terms of the relative gain process $\mathcal{G}$. The terms $(\hat{d}_{h,\epsilon}/d_0)^\gamma$ are canceled; therefore, the spatial path loss does not affect the SIR. This property follows from the planar system model of the narrow-beam LEO with equal spatial path losses for all UEs. However, this also holds for the performance metrics using the spherical model, namely for $\mathring{\text{SIR}} \triangleq \mathring{S}/\mathring{I}$, where $\mathring{S}$ and $\mathring{I}$ are defined in (7); this is a substantial difference from the usual terrestrial models, where the SIR depends strongly on the path loss exponent [18, Eq. (6.64)].

Note that, from Lemma 1, the GP=RGP: the nearest transmitter distance $\|x_0\|$ in $\mathcal{G}$ can be conditioned arbitrarily or have an arbitrary distribution as long as the p.p. of the other transmitters is a HPPP of density λ. It follows that, after decoding and canceling the signal of the nearest UEs, the SIR distribution remains the same for the second nearest transmitters (considered now the nearest). Therefore, for such *successive interference cancellation*, the model describes the SIR at the nearest UEs to their serving SBS and the second nearest, third nearest, and so on. This property is due to the second power exponential path loss function, *i.e.*, the Gaussian antenna gain, that preserves the Poisson property of the RGP (11).

III. Meta Distribution of the SIR

The SIR MD at the typical SBS is the distribution of the r.v. $\mathcal{P}_{\kappa,m}(\theta) \triangleq \mathbb{P}(\text{SIR}_{\kappa,m} > \theta|\Phi)$, and it is defined for $0 \le y \le 1$ as

$$\begin{aligned}\mathbb{P}(\mathcal{P}_{\kappa,m}(\theta) > y) &= \mathbb{P}(\mathbb{P}(\text{SIR}_{\kappa,m} > \theta|\Phi) > y) \\ &= \mathbb{E}_{\Phi}\mathbb{1}(\mathbb{P}(\text{SIR}_{\kappa,m} > \theta|\Phi) > y), \end{aligned} \quad (17)$$

where $\mathbb{1}(\cdot)$ is the indicator function.

The averaging in (17) is taken over the *ensemble* of Φ at the typical location. However, because Φ is ergodic, the ensemble average is equal to the spatial average, given a realization of Φ. In this sense, the SIR MD describes the SBS reliability in a uniform (or homogeneous) constellation. The SIR MD gives the fraction of SBSs that reach reliability y, which is the fraction of time during a short use period that the SIR threshold θ is reached.

A. Moments of the SIR MD

We use multi-indices to simplify the notation. For the nonnegative integer tuples $\Gamma = (\Gamma_1, \Gamma_2, \ldots, \Gamma_m)$ and $B = (B_1, B_2, \ldots, B_m)$, we define the product $B^{\Gamma} = B_1^{\Gamma_1} B_2^{\Gamma_2} \cdots B_m^{\Gamma_m}$, the multinomial coefficient $\binom{b}{\Gamma} = b!/(\Gamma_1!\Gamma_2! \cdots \Gamma_m!)$, and the absolute value $|\Gamma| = \Gamma_1 + \Gamma_2 + \cdots + \Gamma_m$. We are ready to derive the moments of the SIR MD $M^b_{\kappa,m}(\theta) \triangleq \mathbb{E}[\mathcal{P}_{\kappa,m}(\theta)^b]$.

Proposition 1 (Moments of the SIR MD). *The bth moment in a narrow-beam LEO uplink when all transmitters experience Nakagami-m fading is approximately given as a sum over all Γ such that $|\Gamma| = b$:*

$$\begin{aligned} M^b_{\kappa,m}(\theta) &\approx \hat{M}^b_{\kappa,m}(\theta) \\ &\triangleq \sum_{|\Gamma|=b} \binom{b}{\Gamma} \exp\left\{-\tilde{\kappa}\int_0^1 \frac{1 - A(\theta,r)^{\Gamma}}{r} dr\right\} B^{\Gamma}, \end{aligned} \quad (18)$$

where $A_n(\theta, r) = \left(1 + m!^{-1/m}\theta n r\right)^{-m}$ and $B_n = \binom{m}{n}(-1)^{n+1}$, $n = 1, \ldots, m$. For $m = 1$, $\hat{M}^b_{\kappa,m}(\theta) = M^b_{\kappa,m}(\theta)$.

Proof. We utilize the PGFL of the RGP (15). The proof is given in Appendix C. □

For Rayleigh fading, we provide multiple representations (19)-(23) for the moments.

Corollary 1 (Moments of the SIR MD for Rayleigh fading). *With $m = 1$, the expression* (18) *can be further evaluated as follows. The first and the second moments of the* SIR *MD in a narrow-beam LEO uplink, when all transmitters experience Rayleigh fading, are given by (recall that $\hat{M}^b_{\kappa,1}(\theta) = M^b_{\kappa,1}(\theta)$)*

$$M^1_{\kappa,1}(\theta) = (1+\theta)^{-\tilde{\kappa}}, \quad (19)$$

$$M^2_{\kappa,1}(\theta) = e^{-\tilde{\kappa}\theta/(1+\theta)}(1+\theta)^{-\tilde{\kappa}}, \quad (20)$$

respectively. The general moments $b \in \mathbb{C}$ are given by

$$\begin{aligned} M^b_{\kappa,1}(\theta) &= \exp\left\{-\tilde{\kappa}\int_0^1 \left(1 - \frac{1}{(1+\theta r)^b}\right)/r dr\right\} \quad (21) \\ &= \exp\left\{-\theta b\tilde{\kappa}\, {}_3F_2(1,1,1+b;2,2;-\theta)\right\}, \quad (22) \end{aligned}$$

where ${}_3F_2(\cdot)$ is the hypergeometric function. Furthermore, for $b \in \mathbb{N}$,

$$M^b_{\kappa,1}(\theta) = \exp\left\{\frac{\tilde{\kappa}}{(b-1)!}\sum_{k=1}^{b}\begin{bmatrix} b \\ k \end{bmatrix}\text{Li}_{2-k}(-\theta)\right\}, \quad (23)$$

where $\begin{bmatrix} n \\ k \end{bmatrix}$ is the unsigned Stirling number of the first kind, and $\text{Li}_{2-k}(\cdot)$ is the polylogarithm.

Proof. Equation (21) follows from (18) for $m = 1$. The first two moments can be evaluated through elementary integration methods from (21). The derivation of (23) is given in Appendix D. □

As a mathematical curiosity, $\text{Li}_{2-k}(-\theta)$ also has closed-form expressions for $k \ge 3$ [23, Eq. (6.3)], although relatively complicated.

B. Approximation of the SIR MD

Using the moments, we present two ways to approximate the SIR MD: the beta distribution and Chebyshev-Markov Inequalities.

1) The beta distribution

The beta distribution effectively approximates the SIR MD, especially if no *inflection points* exist. If α and β are the shape parameters of the beta distribution, the first and the second moments are given by $\alpha/(\alpha+\beta)$ and $\alpha(\alpha+1)/((\alpha+\beta)(\alpha+\beta+1))$, respectively. Using the expression (18), or in the Rayleigh fading case, (19) and (20) for the first two moments and matching them to the corresponding moments of the beta distribution, we can solve for α and β:

Proposition 2 (Approximation of the SIR MD with the beta distribution). *The parameters α and β for the beta distribution are given as*

$$\begin{aligned} \alpha &= \left(\frac{\hat{M}^1_{\kappa,m}(\theta)(1 - \hat{M}^1_{\kappa,m}(\theta))}{\hat{M}^2_{\kappa,m}(\theta) - \hat{M}^1_{\kappa,m}(\theta)^2} - 1\right)\hat{M}^1_{\kappa,m}(\theta) \\ \beta &= \left(\frac{\hat{M}^1_{\kappa,m}(\theta)(1 - \hat{M}^1_{\kappa,m}(\theta))}{\hat{M}^2_{\kappa,m}(\theta) - \hat{M}^1_{\kappa,m}(\theta)^2} - 1\right)(1 - \hat{M}^1_{\kappa,m}(\theta)) \end{aligned} \quad (24)$$

The SIR MD can be approximated by the beta distribution:

$$\mathbb{P}(\mathcal{P}_{\kappa,m}(\theta) > y) \approx \begin{cases} 1 - I_y(\alpha,\beta), & y \in [0,1], \\ 1, & y < 0, \\ 0, & y > 1, \end{cases} \quad (25)$$

where $I_{(\cdot)}(\alpha,\beta)$ is the regularized incomplete beta function.

2) Chebyshev-Markov inequalities

Given a moment sequence $(\hat{M}^b_{\kappa,m}(\theta))_{b=0}^n$, the order n CM inequalities give the pointwise infimum and supremum

$$\inf_{F \in \mathcal{F}_n} F(y), \quad \sup_{F \in \mathcal{F}_n} F(y) \quad (26)$$

for any $y \in [0,1]$, where $\mathcal{F}_n$ is the set of the distributions that agree with the moment sequence. The inequalities established by the infima and suprema are called the CM inequalities [24, Th. 1]. We use the CM inequalities to validate the theory by comparing the CM inequalities derived from the moments (18) to the simulated SIR MD in the spherical model.

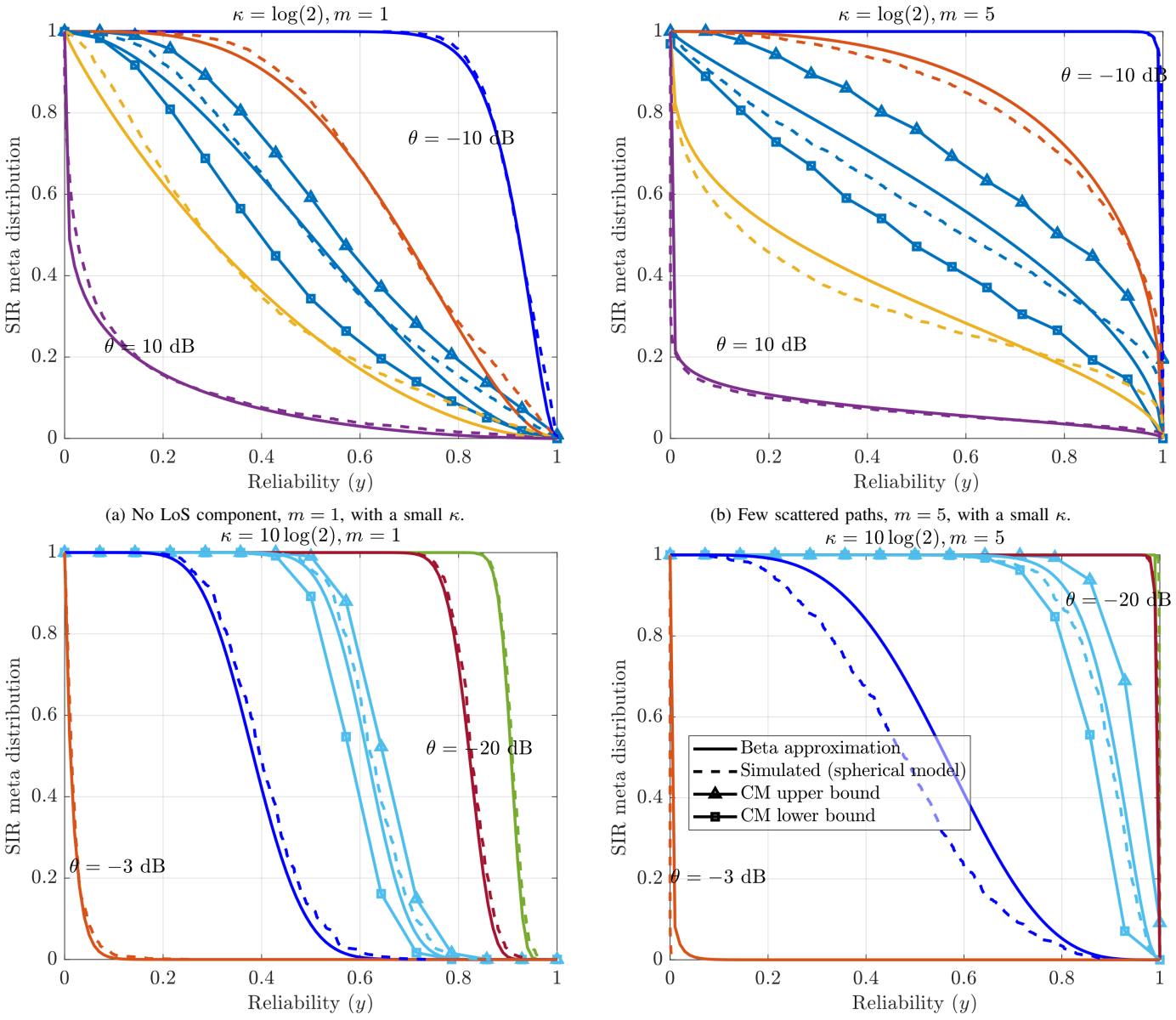

(a) No LoS component, $m = 1$, with a small κ.

(b) Few scattered paths, $m = 5$, with a small κ.

(c) No LoS component, $m = 1$, with a large κ.

(d) Few scattered paths, $m = 5$, with a large κ.

Fig. 5: Simulated SIR MD and the beta distribution approximations with different SIR thresholds θ and fading variables $m \in \{1, 5\}$. We plot the thresholds $\theta \in \{-10, -3, 0, 3, 10\}$ dB and $\theta \in \{-20, -17, -13, -10, -3\}$ dB (from top to bottom) for $\kappa \in \{\log(2), 10\log(2)\}$, respectively. The path loss exponent $\gamma = 2$ (recall that, like in the analysis, this does not notably affect the distribution) and the parameters $\lambda \in 1.9 \cdot \{10^{-3}, 10^{-4}\}/\text{km}^2$, $h = 1200$ km, $\epsilon = 80°$ and $\varphi_{\text{RX}} = 1.6°$ corresponding to $\kappa \in \{\log(2), 10\log(2)\}$, respectively. (Recall that the only essential spatial system parameter is κ. The other parameters have only a minor impact on the simulated values.) Order 15 CM inequalities are depicted for $\theta \in \{0, -13\}$ dB for $\kappa \in \{\log(2), 10\log(2)\}$, respectively.

C. *SIR MD numerical results*

Figure 5 depicts the SIR MDs for varying densities and fading parameters. The beta distribution approximations are shown with the simulated SIR MD $\mathbb{P}(\mathbb{P}(\mathring{\text{SIR}} > \theta|\Theta) > y)$ using the spherical model, $\mathring{\text{SIR}} = \mathring{S}/\mathring{I}$. We also plot order 15 CM inequalities for different θ (we omit the other inequalities to avoid cluttering the figures). The beta distribution approximation is particularly feasible for the Rayleigh fading. One can see that for $\kappa = \log(2)$, the variance in reliability is significant: some SBSs have relatively good reliability, whereas others have a bad connection. In particular, for $m = 5$, $1/5$ of the SBSs reach $\theta = 10$ dB during the use period, and the rest are experiencing an outage at this threshold. On the contrary, for $\kappa = 10\log(2)$, especially in the Rayleigh fading case, the variance in the reliability is small. With $m = 5$, the variance is more considerable for $\theta = -10$ dB. Otherwise, the reliability is near 0 or 1; depending on the SIR threshold needed for the transmission, all SBSs perform very well, or the connection is permanently down.

IV. SIR, SINR AND THROUGHPUT DISTRIBUTIONS

A. *SIR distribution*

The SIR distribution is straightforward to obtain from the SIR MD since the first moment is just the complementary cumulative distribution function (CCDF) $F^{\text{SIR}}_{\kappa,m}(\theta) \triangleq \mathbb{P}(\text{SIR}_{\kappa,m} > \theta) = M^1_{\kappa,m}(\theta)$ of the SIR. We denote $\hat{F}^{\text{SIR}}_{\kappa,m}(\theta) \triangleq$

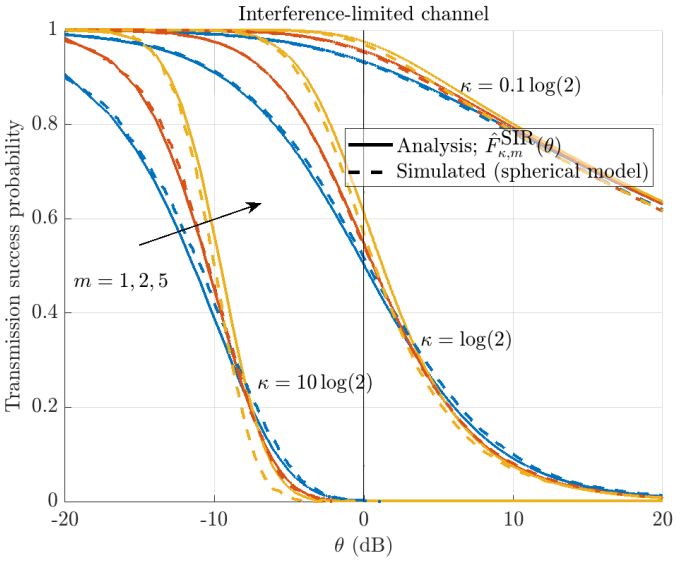

Fig. 6: Simulated SIR distributions using the spherical model and the corresponding theoretical distribution for $\kappa \in \log(2) \cdot \{0.1, 1, 10\}$ and $m \in \{1, 2, 5\}$. The parameters $\gamma = 4$, $h = 600$ km, $\epsilon = 80°$, $\varphi_{\text{RX}} = 1.6°$ and $\lambda \in 7.4 \cdot \{10^{-5}, 10^{-4}, 10^{-3}\}/\text{km}^2$ were used, which match the respective κ. (Recall that the only essential spatial system parameter is κ. The other parameters have only a minor impact on the simulated values.)

$\hat{M}^1_{\kappa,m}(\theta)$ the approximation of the SIR distribution. If θ is the SIR threshold needed for successful transmission, $\hat{F}^{\text{SIR}}_{\kappa,m}(\theta)$ is the *transmission success probability*. We provide multiple representations (27) – (30) for the transmission success probability.

COROLLARY 2 (SIR distribution). *The transmission success probability in a narrow-beam LEO Nakagami-m fading interference-only uplink channel is given for $m \in \{1, 2\}$ by*

$$F^{\text{SIR}}_{\kappa,1}(\theta) = \hat{F}^{\text{SIR}}_{\kappa,1}(\theta) = \hat{M}^1_{\kappa,1}(\theta) = (1+\theta)^{-\tilde{\kappa}}, \tag{27}$$

$$F^{\text{SIR}}_{\kappa,2}(\theta) \approx \hat{F}^{\text{SIR}}_{\kappa,2}(\theta) = \hat{M}^1_{\kappa,2}(\theta)$$
$$= 2e^{-\frac{\sqrt{2}\theta\tilde{\kappa}}{\sqrt{2}\theta+2}} \left(\frac{\theta}{\sqrt{2}}+1\right)^{-\tilde{\kappa}} - e^{-\frac{\sqrt{2}\theta\tilde{\kappa}}{\sqrt{2}\theta+1}} \left(\sqrt{2}\theta+1\right)^{-\tilde{\kappa}}, \tag{28}$$

respectively. The expression for general $m \in \mathbb{N}$ is

$$F^{\text{SIR}}_{\kappa,m}(\theta) \approx \hat{F}^{\text{SIR}}_{\kappa,m}(\theta) = \hat{M}^1_{\kappa,m}(\theta)$$
$$= \sum_{n=1}^{m} \exp\left\{-\tilde{\kappa}\int_0^1 \frac{1-(1+C_n\theta r)^{-m}}{r} dr\right\} B_n \tag{29}$$

$$= \sum_{n=1}^{m} \exp\left\{\frac{\tilde{\kappa}}{(m-1)!}\sum_{k=1}^{m} \begin{bmatrix} m \\ k \end{bmatrix} \text{Li}_{2-k}\left(-C_n\theta\right)\right\} B_n, \tag{30}$$

where $\begin{bmatrix} m \\ k \end{bmatrix}$ is the unsigned Stirling number of the first kind, $B_n = \binom{m}{n}(-1)^{n+1}$ and $C_n = (m!)^{-1/m} n$, $n = 1, \ldots, m$. In the Rayleigh fading case, $F^{\text{SIR}}_{1,\kappa}(\theta) = \hat{F}^{\text{SIR}}_{1,\kappa}(\theta)$. Recall that the exponent also has the hypergeometric representation as in (22).

Proof. The first moment follows directly by substituting $b = 1$ to (18). The polylogarithmic expression of the integral in (29) is derived in Appendix D. The Rayleigh case follows directly from (19), and the $m = 2$ case follows from substituting $\text{Li}_1(-C_n\theta) = -\log(1+C_n\theta)$ and $\text{Li}_0(-C_n\theta) = -C_n\theta/(1+C_n\theta)$ to (30). □

With Rayleigh fading, the SIR distribution (27) is a Lomax (Pareto Type II) distribution with the shape parameter $\tilde{\kappa}$.

*1) **Average SIR and variance***

Fading has little effect on the first moment of the SIR (cf. Section IV-C). Hence, an expression for the average SIR over the uniformly distributed SBSs is simply given by integrating the SIR CCDF in the Rayleigh fading case over the positive half-line:

$$\mathbb{E}(\text{SIR}_{\kappa,m}) \approx \mathbb{E}(\text{SIR}_{\kappa,1}) = \int_0^\infty F^{\text{SIR}}_{\kappa,1}(y)dy = \frac{1}{\tilde{\kappa}-1}, \tag{31}$$

for $\tilde{\kappa} > 1$. The mean is divergent for $\tilde{\kappa} \leq 1$, that is, $\kappa \leq \log(2)$: On average, having less than $\log(2)$ UEs inside the -3 dB footprint, a significant fraction of SBSs have a very high SIR, and a significant fraction has a low SIR. Consequently, the expected SIR and the variance are undefined. Under this threshold, the interference-only channel is inadequate in modeling the mean SINR even for minimal noise values—physically bounded by the noise. Furthermore, the *nth* moment of the Lomax distribution exists if and only if $\tilde{\kappa} > n$, implying that the variance of the SIR is infinite for $1 < \tilde{\kappa} \leq 2$ and undefined for $0 < \tilde{\kappa} \leq 1$.

*2) **Decay rate of the tail***

The asymptotic decay rate helps to gain insight into the SIR distribution. Heuristically, we know that $\lim_{y\to\infty} \text{Li}_{2-k}(-C_n y) = 0$ for $k > 2$; otherwise, the term $\exp\{\text{Li}_{2-2}(-C_n y)\} = \exp\{-C_n y/(1+C_n y)\}$ decays the slowest in (30). Estimating the polylogarithm, the asymptotic decay rate

$$\rho_{\text{SIR}} \triangleq -\lim_{y\to\infty} \frac{\log(\hat{F}^{\text{SIR}}_{\kappa,m}(y))}{y} \leq 0. \tag{32}$$

The condition $\rho_{\text{SIR}} = 0$ is equivalent to the heavy-tailed distribution in that the exponential moment $\mathbb{E}(e^{t\text{SIR}_{\kappa,m}})$ is divergent for any $t > 0$ [25, Th. 2.6]. The SIR distribution has a slowly decaying tail for all κ and m. In practice, one may expect frequent *outliers* in the SIR.

*3) **SIR numerical results***

In Figure 6, we plot the theoretical and simulated transmission success probability for various κ: $\hat{F}^{\text{SIR}}_{\kappa,m}(\theta)$ and $\mathbb{P}(\text{SIR} > \theta)$, respectively. The Lomax distribution (27) approximates all SIR distributions in the tail. It can generally be used to model the SIR distribution in the simple coverage region $\theta \geq 1$. Other than the tail distribution, the Lomax distribution gives pessimistic values for the probability of coverage.

B. SINR distribution

The tail behavior observed in the model is due to the lack of sidelobes or noise. In this section, we add a constant dimensionless noise power term $W > 0$ to I and analyze the $\text{SINR}_{\kappa,W,m} \triangleq S/(I+W)$. Define the transmission success probability $F^{\text{SINR}}_{\kappa,W,m}(\theta) \triangleq \mathbb{P}(\text{SINR}_{\kappa,W,m} > \theta)$.

PROPOSITION 3 (SINR distribution). *In the interference-plus-noise-limited channel, for $m = 1$;*

$$F^{\text{SINR}}_{\kappa,W,1}(\theta) = (1+\theta)^{-\tilde{\kappa}} E_{\tilde{\kappa}+1}\left(W(\hat{d}_{h,\epsilon}/d_0)^\gamma\theta\right)\tilde{\kappa}, \tag{33}$$

and for general $m \in \mathbb{N}$;

$$F^{\text{SINR}}_{\kappa,W,m}(\theta) \approx \hat{F}^{\text{SINR}}_{\kappa,W,m}(\theta) \triangleq \sum_{n=1}^{m} \exp\left\{ \frac{\tilde{\kappa}}{(m-1)!} \sum_{k=1}^{m} \begin{bmatrix} m \\ k \end{bmatrix} \text{Li}_{2-k}\left(-C_n\theta\right) \right\} B_n \cdot E_{\kappa+1}\left(mC_nW(\hat{d}_{h,\epsilon}/d_0)^{\gamma}\theta\right)\tilde{\kappa}, \tag{34}$$

where $E_{\tilde{\kappa}+1}(\cdot)$ is the generalized exponential integral, $\begin{bmatrix} m \\ k \end{bmatrix}$ is the unsigned Stirling number of the first kind, $B_n = \binom{m}{n}(-1)^{n+1}$ and $C_n = (m!)^{-1/m}n$, $n = 1, \ldots, m$. Recall that the exponent has the integral and hypergeometric representations (21) *and* (22)*, respectively.*

Proof. We give the proof with Rayleigh fading. The proof for the general m is analogous by using the exponential form to approximate the CCDF of the gamma distributed g_{x_0}, similar to the derivation given in Appendix C.

$$\begin{aligned} F^{\text{SINR}}_{\kappa,W,1}(\theta) &= \mathbb{P}\left(g_{x_0} > \sum_{x\in\mathcal{G}} g_x x + \frac{W(\hat{d}_{h,\epsilon}/d_0)^{\gamma}\theta}{G[D_{h,\epsilon}\|x_0\|]} \right) \\ &\overset{(a)}{=} \mathbb{E}_{\Phi}\mathbb{E}_g\left(e^{-\theta\sum_{x\in\mathcal{G}} g_x x}\right)\mathbb{E}_{\Phi}\left(e^{-W(\hat{d}_{h,\epsilon}/d_0)^{\gamma}\theta/G[D_{h,\epsilon}\|x_0\|]}\right) \\ &\overset{(b)}{=} \mathbb{E}\prod_{x\in\mathcal{G}} \frac{1}{1+\theta x} E_{\tilde{\kappa}+1}\left(W(\hat{d}_{h,\epsilon}/d_0)^{\gamma}\theta\right)\tilde{\kappa} \\ &\overset{(c)}{=} (1+\theta)^{-\tilde{\kappa}} E_{\tilde{\kappa}+1}\left(W(\hat{d}_{h,\epsilon}/d_0)^{\gamma}\theta\right)\tilde{\kappa}. \end{aligned} \tag{35}$$

(a) follows from the equivalence of the GP and RGP, and thus, $\mathcal{G}$ is independent of the served UE x_0, and the expectation of the exponential term (that follows from the CCDF of the exponential r.v. g_{x_0}) can be separated into the product. In (b), we used the Laplace transform $\mathcal{L}_{1/G[D_{h,\epsilon}\|x_0\|]}(s) \triangleq \mathbb{E}\exp\{-s/G[D_{h,\epsilon}\|x_0\|]\} = E_{\tilde{\kappa}+1}(s)\tilde{\kappa}$ of the inverse largest gain, which can be derived directly from the definition of the Laplace transform using the (derivative of the) CDF $\mathbb{P}(1/G[D_{h,\epsilon}\|x_0\|] < r) = 1 - (1/r)^{\tilde{\kappa}}$, which is not difficult to establish by using the nearest-neighbor distribution of the PPP on $\mathbb{R}^2$ [7, Example 2.11]. (c) follows by evaluating the PGFL (15) of $\mathcal{G}$. □

For $W = 0$, we directly retrieve the SIR distribution; $F^{\text{SINR}}_{\kappa,0,m}(\theta) = F^{\text{SIR}}_{\kappa,m}(\theta)$.

*1) **SINR numerical results***

In Figure 7, we plot the theoretical SINR distribution and the simulated $\mathbb{P}(\text{SINR} > \theta) \triangleq \mathbb{P}(\mathring{S}/(\mathring{I}+W) > \theta)$ distribution for various κ. The noise is set to $W = 0.2 \cdot (d_{h,\epsilon}/d_0)^{-\gamma}$, or equivalently, measured in decibels w.r.t. the average signal strength of a UE at o is $10\log_{10}(W/(\hat{d}_{h,\epsilon}/d_0)^{-\gamma}) = -7$ dB. Contrary to the SIR distribution, smaller κ does not necessarily produce better coverage probabilities: With a small κ, the served UE is likely to be far away from the SBS, and because of the path loss, the noise will restrict the SINR. Approximately at $\kappa = \log(2)$, the coverage probabilities are at maximum.

The error, particularly visible for $\kappa = 0.1\log(2)$, is due to the low elevation angle $\epsilon = 45°$, which causes a significant difference between $\hat{d}_{h,\epsilon}$ and $d_{h,\epsilon}$ and a significantly elliptical main lobe footprint in the simulations.

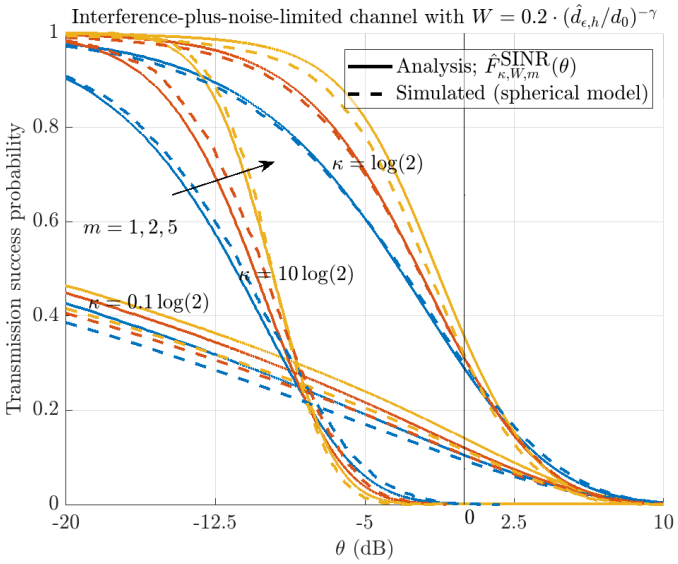

Fig. 7: Simulated SINR distributions using the spherical model and the corresponding theoretical distribution for $\kappa \in \log(2) \cdot \{0.1, 1, 10\}$ and $m \in \{1, 2, 5\}$. The parameters $\gamma = 2$, $h = 200$ km, $\epsilon = 45°$, $\varphi_{\text{RX}} = 1.6°$, $W = (\hat{d}_{h,\epsilon}/d_0)^{-\gamma}$ and $\lambda \in 1.8 \cdot \{10^{-4}, 10^{-3}, 10^{-2}\}/\text{km}^2$ were used, which match the respective κ. (Recall that the only essential spatial system parameter is κ. The other parameters have only a minor impact on the simulated values.)

The simple analytic expression $F^{\text{SINR}}_{\kappa,W,1}(\theta)$ (33) derived for the exponential power fading can be used to model the SINR tail distribution, generally in the simple coverage region $\theta \geq 1$. Other than the tail distribution, $F^{\text{SINR}}_{\kappa,W,1}(\theta)$ gives pessimistic values for the probability of coverage.

C. Throughput distribution

The instantaneous channel capacity is defined by $\mathcal{T}_{\kappa,W,m} \triangleq \log(1 + \text{SINR}_{\kappa,W,m})/\log(2)$ [18, Eq. (7.19)]. As observed from Figure 8, the type of fading has a negligible effect on the average normalized throughput, or spectral efficiency. Being simplest, we derive the throughput for the Rayleigh fading and denote $\hat{\tau}_{\kappa,W} \triangleq \mathbb{E}\left(\mathcal{T}_{\kappa,W,1}\right)$. For other fading cases, the exact values can be derived similarly to $\hat{\tau}_{\kappa,W}$.

*1) **Average throughput in the interference-limited channel***

Recall the SIR distribution $F^{\text{SIR}}_{\kappa,1}(\cdot)$ (27). Without noise, one can evaluate the average throughput:

$$\begin{aligned} \hat{\tau}_{\kappa,0} &= \frac{1}{\log(2)}\int_0^{\infty} \mathbb{P}(\text{SIR}_{\kappa,1} > e^t - 1)dt \\ &= \int_0^{\infty} \frac{F^{\text{SIR}}_{\kappa,1}(e^t-1)}{\log(2)}dt \overset{(a)}{=} \int_0^{\infty} \frac{(1+v)^{-\tilde{\kappa}-1}}{\log(2)}dv = 1/\kappa, \end{aligned} \tag{36}$$

where we use the integration by substitution $v = e^t - 1$ in (a). Recall that $\kappa = \tilde{\kappa}\log(2)$ (13) is the mean number of UEs inside the -3 dB footprints of the SBSs.

*2) **Average throughput in the interference-plus-noise-limited channel***

Recall the SINR distribution $F^{\text{SINR}}_{\kappa,W,1}(\cdot)$ (33). With noise, similar to (36), the average throughput is given by

$$\hat{\tau}_{\kappa,W} = \frac{1}{\log(2)} \int_0^\infty \frac{F^{\text{SINR}}_{\kappa,W,1}(v)}{1+v} dv$$
$$= \frac{1}{\log(2)} \int_0^\infty (1+v)^{-\tilde{\kappa}-1} E_{\tilde{\kappa}+1}\left(W(\hat{d}_{h,\epsilon}/d_0)^\gamma v\right) \tilde{\kappa} dv. \quad (37)$$

Throughout the rest of the work, let us (vaguely) mean by *moderate noise* that the expected SNR is around 1 for the served UE at o, *i.e.*, $W \approx (\hat{d}_{h,\epsilon}/d_0)^{-\gamma}$, or equivalently, the decibels w.r.t. the average signal strength of a UE at o is $10\log_{10}(W/(\hat{d}_{h,\epsilon}/d_0)^{-\gamma}) \approx 0$ dB.

$\hat{\tau}_{\kappa,W}$ is complex to evaluate other than numerically for $W > 0$. For this reason, we will utilize two approximations of the exponential integral $E_{\tilde{\kappa}+1}(y)$ to help evaluate the integral (37). The following closed-form approximation of the average throughput is simple yet suitable for moderate or large noise. It is pessimistic except, not visibly, optimistic for small κ. Furthermore, $\mathfrak{T}_{\kappa,W} \sim \hat{\tau}_{\kappa,W} \sim \hat{\tau}_{\kappa,0} = 1/\kappa, \kappa \to \infty$.

APPROXIMATION 1 (A simple approximation of the average throughput). For moderate to large noise, the average normalized throughput can be approximated by

$$\hat{\tau}_{\kappa,W} \approx \mathfrak{T}_{\kappa,W} \triangleq \frac{\tilde{\kappa}}{(\tilde{\kappa}+1)(\tilde{\kappa}+W(\hat{d}_{h,\epsilon}/d_0)^\gamma)\log(2)}. \quad (38)$$

Proof. First, we use the first order asymptotic approximation $E_{\tilde{\kappa}+1}(y) \approx e^{-y}/(\tilde{\kappa}+1)$ [26, Th. 51] for $E_{\tilde{\kappa}+1}(W(\hat{d}_{h,\epsilon}/d_0)^\gamma v)$ to help to evaluate (37):

$$\hat{\tau}_{\kappa,W} \approx \frac{\tilde{\kappa} e^{W(\hat{d}_{h,\epsilon}/d_0)^\gamma} E_{\tilde{\kappa}+1}(W(\hat{d}_{h,\epsilon}/d_0)^\gamma)}{(\tilde{\kappa}+1)\log(2)}.$$

The final result is achieved by using approximation $E_{\tilde{\kappa}+1}(y) \approx e^{-y}/(\tilde{\kappa}+y)$ instead of the exponential integral. □

*3) **Optimal average throughput***

We can solve $d\mathfrak{T}_{\kappa,W}/d\kappa = 0$ for κ, and get the maximizing

$$\kappa_\tau^{\max} \triangleq \arg\max\{\kappa : \mathfrak{T}_{\kappa,W}\} = \sqrt{W(\hat{d}_{h,\epsilon}/d_0)^\gamma}\log(2). \quad (39)$$

For $W = (\hat{d}_{h,\epsilon}/d_0)^{-\gamma}$, $\kappa_\tau^{\max} = \log(2)$: This follows the intuition that, with moderate noise, the performance metric is maximized at UE density where the expected SIR approaches infinity (recall (31)). By the void probability of the PPP, at $\kappa = \log(2)$, the served UE is inside the -3 dB footprint at the probability $1 - \exp\{-\log(2)\} = 1/2$ and inside the -10 dB footprint at the probability $1 - \exp\{-\log(10)\} = 9/10$—this reflects a physically sensible cell size. For $W \to 0$, we approach the interference-only channel, and $\kappa_\tau^{\max} = 0$ reflects the no-noise-nor-interferers case, trivially maximizing the throughput (recall (16) and the independence of the SIR from the distance to the served UE).

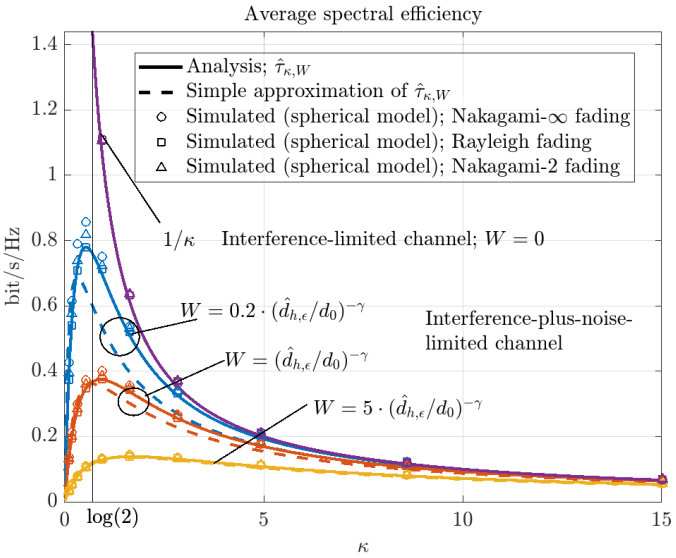

Fig. 8: Simulated actual and the theoretical expected normalized throughput for $\kappa \in [0, 15]$ and $W \in \{0, 0.2, 1, 5\} \cdot (\hat{d}_{h,\epsilon}/d_0)^{-\gamma}$ (from top to bottom) and $m \in \{1, 2, \infty\}$. The parameters $\gamma = 4$, $h = 1200$ km, $\epsilon = 85°$, $\varphi_{\text{RX}} = 1.6$ and $\lambda \in [0, 4.2 \cdot 10^{-3}]/\text{km}^2$ were used, which match the respective κ. (Recall that the only essential spatial system parameter is κ. The other parameters have only a minor impact on the simulated values.)

*4) **Average throughput numerical results***

In Figure 8, we plot the average throughput for various κ and W and compare the theoretical $\mathbb{E}(\mathcal{T}_{\kappa,0,m}) \approx 1/\kappa$ and $\mathbb{E}(\mathcal{T}_{\kappa,W,m}) \approx \hat{\tau}_{\kappa,W}$ to the simulated $\mathbb{E}\log(1+\text{SIR})$ and $\mathbb{E}\log(1+\text{SINR})$, respectively. We show the simulated values in Rayleigh, Nakagami-2, and Nakagami-∞ scenarios. The simulated results are similar in all fading scenarios. The simple approximation $\mathfrak{T}_{\kappa,W}$ is very good for moderate and large noise. For $W = 0.2 \cdot (\hat{d}_{h,\epsilon}/d_0)^{-\gamma}$, the interference-only expression (36) closely approximates the throughput for $\kappa > 1$. The optimal κ is close to $\log(2)$ with all depicted noise values, as implied by (39). Further, the average spectral efficiency is relatively flat w.r.t. κ for large noise.

Recall the SIR MD analysis in Section III and Figure 5: Even though $\kappa \approx \log(2)$ maximizes the *average* throughput for moderate noise, the SBS reliability significantly vary at this κ. The same insight is reflected in the undefined or infinite variance of the Lomax SIR distribution (27) for $\kappa \leq 2\log(2)$.

V. CONCLUSIONS

We derived the SIR and its meta distribution (MD), as well as the SINR distribution and the expected throughput in a narrow-beam LEO uplink Nakagami channel in the presence of Poisson distributed interferers. Some expressions of the distributions are very simple; the SIR follows a Lomax distribution in the simple coverage region (and in the general coverage region for the Rayleigh fading), and the average throughput is proportional to the inverse of the density of the user equipments (UEs) in the interference-only channel. In the interference-plus-noise-limited channel, we obtained a UE density maximizing the average throughput. Regardless of the antenna gain width, altitude, or elevation angle, with moderate noise levels, the maximizing density approximately

corresponds to, on average, $\kappa \approx \log(2)$ UEs inside the satellite base stations (SBS) -3 dB footprints. On the contrary, it was observed that to maintain a consistent user experience, we must make the distribution of UEs dense because of the highly varying received signal strengths from the UEs if they are sparsely located (the Lomax distribution representing the SIR distribution has a divergent variance for $\kappa \leq 2\log(2)$).

In other words, maximizing average performance by optimizing the UE density comes with the cost of reduced user fairness. In light of the presented model, a possible solution for maintaining a consistent user experience is to increase the density of the constellation: should we consider that each UE has a serving satellite, the density of UEs determines the satellite constellation density directly. Furthermore, interference cancellation and combination can be implemented so that a single SBS can serve single or even multiple densely located UEs with satisfactory SIR and SINR. Alternatively, it is possible to complement the satellite network with a terrestrial network that serves the UEs during an outage in the LEO network. This work helps to characterize the achievable average performance and the SBS reliability with different co-channel UE densities, altitudes, elevation angles, and SBS antenna gain widths.

The paper introduces a novel and analytically tractable framework for modeling narrow-beam LEO communications using stochastic geometry. The approach yields simpler results than existing models in the literature while maintaining high accuracy. Future research could improve the model's applicability by investigating explicit shadowing effects and the more realistic distribution of UEs, particularly regarding the impact of interference on the narrow-beam and narrowband LEO performance. Furthermore, studying interference cancellation and signal combination within the framework would be interesting. The proposed model and the insights of this paper also apply to the downlink, considering that the SBS footprint locations on the Earth are distributed according to the HPPP.

Appendix A
Scaling Constant

See Figure 9. We have that $\zeta_z = \tan^{-1}(z/h)$. The derivative of φ_x around o is given approximately by

$$\frac{d}{d\|x\|}\varphi_x = \frac{d}{dz}\zeta_z = \frac{d\tan^{-1}(z/h)}{dz} = \frac{h}{h^2+z^2}$$
$$\overset{(a)}{\approx} \frac{h}{h^2 - h^2 + \hat{d}_{h,\epsilon}^2} \overset{(b)}{=} \frac{h}{h^2/\sin^2(\epsilon)} = \frac{\sin^2(\epsilon)}{h} = D_{h,\epsilon}, \quad (40)$$

where (a) follows from Pythagoras's theorem, and (b) is standard trigonometry.

Appendix B
Geometry of the Spherical System Model

See Figure 10. Directly from the law of cosines, we have

$$d_{h,\epsilon}(\xi) = \sqrt{R_\oplus^2 + (R_\oplus + h)^2 - 2R_\oplus(R_\oplus + h)\cos(\xi)}. \quad (41)$$

Furthermore, we may derive the relation between ϵ and ξ: The law of cosines states that

$$(R_\oplus + h)^2 = d_{h,\epsilon}(\xi)^2 + R_\oplus^2 - 2d_{h,\epsilon}(\xi)R_\oplus\cos(\pi/2+\epsilon), \quad (42)$$

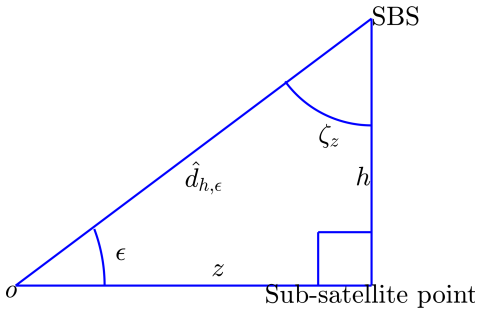

Fig. 9: Geometric interpretation of the variables in Appendix A

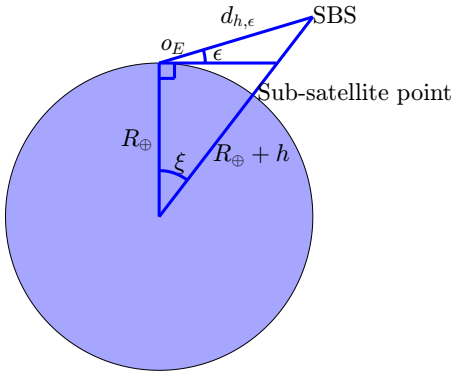

Fig. 10: Sketch of the geometry of the spherical model

which is analytically solvable for ξ.

Appendix C
Moments of the SIR MD with Nakagami Fading

The moments of the SIR MD are derived as follows.

$$M_{\kappa,m}^{(b)}(\theta) = \mathbb{E}\left[\mathbb{P}\left(g_{x_0} > \theta\sum_{x\in\mathcal{G}} g_x x \middle| \Phi\right)^b\right]$$
$$\overset{(a)}{\approx} \mathbb{E}\Bigg[\Bigg(1- \mathbb{E}_g\left[\left(1-\exp\left\{-m(m!)^{-1/m}\theta\sum_{x\in\mathcal{G}} g_x x\right\}\right)^m\right]\Bigg)^b\Bigg]$$
$$\overset{(b)}{=} \mathbb{E}\Bigg[\Bigg(\sum_{n=1}^{m}\binom{m}{n}(-1)^{n+1}\cdot \mathbb{E}_g \exp\left\{-nm(m!)^{-1/m}\theta\sum_{x\in\mathcal{G}} g_x x\right\}\Bigg)^b\Bigg]$$
$$\overset{(c)}{=} \sum_{\substack{k_1+\cdots+k_m=b;\\ k_1,\ldots,k_m\geq 0}} \binom{b}{k_1,\ldots,k_m}\cdot \exp\left\{-\tilde{\kappa}\int_0^1 \frac{\left[1-\prod_{n=1}^m\left(1+(m!)^{-1/m}\theta n r\right)^{-k_n m}\right]}{r}dr\right\}\cdot \prod_{n=1}^{m}\binom{m}{n}^{k_n}(-1)^{k_n(n+1)}. \quad (43)$$

In (a), we use the upper bound for the incomplete gamma function presented in the proof of Theorem 2 in [27]. In (b),

we use the binomial theorem. In (c), we use the multinomial theorem and the Laplace transform of the gamma distribution and PGFL (15) of the GP. We denote (43) as $\hat{M}^{(b)}_{\kappa,m}(\theta)$. With $m=1$, the approximation is exact: $M^{(b)}_{\kappa,m}(\theta)=\hat{M}^{(b)}_{\kappa,m}(\theta)$.

APPENDIX D
POLYLOGARITHMIC REPRESENTATION

It is straightforward to see that for $m=1$, the moment (43) can be expressed with an exponential with the following integral, which is further represented as the generalized hypergeometric function.

$$\int_0^1 \left(1-\frac{1}{(1+\theta r)^b}\right)/r dr = \theta b\, {}_3F_2(1,1,1+b;2,2;-\theta) \tag{44}$$

for $b\in\mathbb{C}, \theta\in\mathbb{C}\setminus\{-1\}$. Furthermore, the hypergeometric series have a polylogarithmic representation. Using the definition of the hypergeometric series, for $|\theta|<1$ and $b\in\mathbb{N}$;

$$\begin{aligned}
&{}_3F_2(1,1,1+b;2,2;-\theta) = \sum_{n=0}^{\infty}\frac{(1)_n(1)_n(1+b)_n}{(2)_n(2)_n}\frac{(-\theta)^n}{n!}\\
&=\sum_{n=0}^{\infty}\frac{(1+b)_n}{(n+1)^2 n!}(-\theta)^n = \frac{1}{b!}\sum_{n=0}^{\infty}\frac{(n+1)_b}{(n+1)^2}(-\theta)^n\\
&\overset{(a)}{=}\frac{1}{b!}\sum_{n=0}^{\infty}\frac{\sum_{k=0}^{b}\left[{b\atop k}\right](n+1)^k}{(n+1)^2}(-\theta)^n\\
&=\frac{1}{b!}\sum_{k=0}^{b}\left[{b\atop k}\right]\sum_{n=0}^{\infty}\frac{(-\theta)^n}{(n+1)^{2-k}} \overset{(b)}{=} -\frac{1}{b!}\sum_{k=0}^{b}\left[{b\atop k}\right]\frac{\mathrm{Li}_{2-k}(-\theta)}{\theta}.
\end{aligned} \tag{45}$$

In (a), we used the expansion of the rising Pochhammer factorial; in (b), we used the definition of the polylogarithm. The expression can be generalized for $\theta\in\mathbb{C}\setminus\{-1\}$ through the analytic continuation of the polylogarithm. [4]

REFERENCES

[1] M. Höyhtyä, S. Boumard, A. Yastrebova, P. Järvensivu, M. Kiviranta, and A. Anttonen, "Sustainable satellite communications in the 6G era: A european view for multilayer systems and space safety," *IEEE Access*, vol. 10, pp. 99 973–100 005, 2022.

[2] M. Jia, X. Gu, Q. Guo, W. Xiang, and N. Zhang, "Broadband hybrid satellite-terrestrial communication systems based on cognitive radio toward 5G," *IEEE Wireless Communications*, vol. 23, no. 6, pp. 96–106, 2016.

[3] 3GPP, "Solutions for NR to support non-terrestrial networks (NTN), TR 38.821," 3GPP, Tech. Rep., 2023.

[4] M. Haenggi, "The meta distribution of the SIR in Poisson bipolar and cellular networks," *IEEE Transactions on Wireless Communications*, vol. 15, no. 4, pp. 2577–2589, 2016.

[5] Y. Sun and Z. Ding, "A fine grained stochastic geometry-based analysis on LEO satellite communication systems," *IEEE Networking Letters*, vol. 5, no. 4, pp. 237–240, 2023.

[6] H. Lin, C. Zhang, Y. Huang, R. Zhao, and L. Yang, "Fine-grained analysis on downlink LEO satellite-terrestrial mmwave relay networks," *IEEE Wireless Communications Letters*, vol. 10, no. 9, pp. 1871–1875, 2021.

[7] M. Haenggi, *Stochastic geometry for wireless networks*. Cambridge: Cambridge University Press, 2013.

[4]To the best of our knowledge, the interesting connection between the polylogarithm and the generalized hypergeometric function (45) is not presented in other sources except for the special case of $b=0$ [28].

[8] R. Wang, M. A. Kishk, and M.-S. Alouini, "Ultra-dense LEO satellite-based communication systems: A novel modeling technique," *IEEE Communications Magazine*, vol. 60, no. 4, pp. 25–31, 2022.

[9] S. Wang, J. Song, X. Miao, and G. Pan, *Understanding Satellite Communications: The Stochastic Geometry Perspective*, 1st ed. Singapore: Springer, 2024.

[10] A. Yastrebova, I. Angervuori, N. Okati, M. Vehkaperä, M. Höyhtyä, R. Wichman, and T. Riihonen, "Theoretical and simulation-based analysis of terrestrial interference to LEO satellite uplinks," in *GLOBECOM 2020 - 2020 IEEE Global Communications Conference*, 2020, pp. 1–6.

[11] I. Angervuori and R. Wichman, "A closed-form approximation of the SIR distribution in a LEO uplink channel," in *2022 IEEE Globecom Workshops (GC Wkshps): Workshop on Cellular UAV and Satellite Communications, Rio de Janeiro, Brazil*, 2022.

[12] H. Jia, C. Jiang, L. Kuang, and J. Lu, "An analytic approach for modeling uplink performance of mega constellations," *IEEE Transactions on Vehicular Technology*, vol. 72, no. 2, pp. 2258–2268, 2023.

[13] H. Jia, Z. Ni, C. Jiang, L. Kuang, and J. Lu, "Uplink interference and performance analysis for megasatellite constellation," *IEEE Internet of Things Journal*, vol. 9, no. 6, pp. 4318–4329, 2022.

[14] B. Al Homssi and A. Al-Hourani, "Optimal beamwidth and altitude for maximal uplink coverage in satellite networks," *IEEE Wireless Communications Letters*, vol. 11, no. 4, pp. 771–775, 2022.

[15] B. A. Homssi and A. Al-Hourani, "Modeling uplink coverage performance in hybrid satellite-terrestrial networks," *IEEE Communications Letters*, vol. 25, no. 10, pp. 3239–3243, 2021.

[16] A. Talgat, M. A. Kishk, and M.-S. Alouini, "Stochastic geometry-based uplink performance analysis of IoT over LEO satellite communication," *IEEE Transactions on Aerospace and Electronic Systems*, vol. 60, no. 4, pp. 4198–4213, 2024.

[17] C. Li, Z. Fang, Y. Wang, and C. Sun, "An approach for interference modeling and analysis of low orbit satellite internet," in *2023 IEEE 23rd International Conference on Communication Technology (ICCT)*, 2023, pp. 1178–1184.

[18] B. Błaszczyszyn, M. Haenggi, P. Keeler, and S. Mukherjee, *Stochastic Geometry Analysis of Cellular Networks*. Cambridge University Press, 2018.

[19] M. Albulet, "SpaceX V-band non-geostationary satellite system," Space Exploration Technologies Corp., Tech. Rep. SAT-LOA-20170301-00027, 2017. [Online]. Available: https://fcc.report/IBFS/SAT-LOA-20170301-00027/1190019.pdf

[20] 3GPP, "Study on new radio (NR) to support non-terrestrial networks (release 15), TR 38.811," 3GPP, Tech. Rep., 2020.

[21] International Telecommunication Union, "Satellite antenna radiation patterns for non-geostationary orbit satellite antennas operating in the fixed-satellite service below 30 GHz," ITU-R, Recommendation S.1528, 2001. [Online]. Available: https://www.itu.int/dms_pubrec/itu-r/rec/s/R-REC-S.1528-0-200106-I!!PDF-E.pdf

[22] M. Haenggi, "Simalysis: Symbiosis of simulation and analysis," https://stogblog.net/2020/10/15/simalysis-symbiosis-of-simulation-and-analysis/, October 2020, accessed: 2024-07-12.

[23] D. Wood, "The computation of polylogarithms," University of Kent, Computing Laboratory, University of Kent, Canterbury, UK, Tech. Rep. 15-92*, June 1992. [Online]. Available: http://www.cs.kent.ac.uk/pubs/1992/110

[24] X. Wang and M. Haenggi, "The Chebyshev-Markov inequalities," University of Notre Dame, Tech. Rep. cm22, 2022, accessed: 2024-09-2. [Online]. Available: https://www3.nd.edu/~mhaenggi/pubs/techreport_cm22.pdf

[25] S. Foss, D. Korshunov, and S. Zachary, *An Introduction to Heavy-Tailed and Subexponential Distributions*, 2nd ed., ser. Springer Series in Operations Research and Financial Engineering. New York, NY: Springer Nature, 2013.

[26] G. Navas-Palencia, "Fast and accurate algorithm for the generalized exponential integral $E_v(x)$ for positive real order," *Numerical Algorithms*, vol. 77, 02 2018.

[27] H. Alzer, "On some inequalities for the incomplete gamma function," *Math. Comput.*, vol. 66, pp. 771–778, 1997. [Online]. Available: https://api.semanticscholar.org/CorpusID:16808088

[28] C. Candab, "A simple proof of ${}_3F_2(1,1,1;2,2;\rho) = \mathrm{dilog}(1-\rho)/\rho$," 2012, accessed: 2024-09-18. [Online]. Available: https://users.metu.edu.tr/ccandan/pub_dir/hyper_rel.pdf

APPENDIX E
BIOGRAPHY SECTION

Ilari Angervuori received the B.Sc. and M.Sc. degrees in applied mathematics with excellent results from the University of Helsinki, Finland, in 2016 and 2018, respectively. Since 2018, he has been with the School of Electrical Engineering, Aalto University—initially as a research assistant and then as a Ph.D. degree candidate under the supervision of Prof. Risto Wichman. His Ph.D. research subject is stochastic geometry in LEO networks. He thrives on tractable system models and clear analytical insights regarding the nature and performance of terrestrial-LEO communication. He is one of the pioneering authors in stochastic geometry modeling of LEO, mostly specialized in the uplink, and has been well-recognized and cited. From the summer of 2023 to the winter of 2024, he was a visiting researcher at the University of Notre Dame under the supervision of Prof. Martin Haenggi. Other aerial base stations, heterogeneous networks, including small cells and mmWaves, MIMO, intelligent reflecting surfaces, and their adaptations in aerial communications are in his interest—only some to mention—and he is currently looking for new challenges and opportunities in the industry or academia, particularly regarding the system-level (and why not link-level) design and modeling. He believes in global connectivity among the people to better the world, and the environmental and ethical factors further challenge the development of communication systems.

Martin Haenggi received the Dipl.-Ing. (M.Sc.) and Dr.sc.techn. (Ph.D.) degrees in electrical engineering from the Swiss Federal Institute of Technology in Zurich (ETHZ) in 1995 and 1999, respectively. Currently he is the Freimann Professor of Electrical Engineering and a Concurrent Professor of Applied and Computational Mathematics and Statistics at the University of Notre Dame, Indiana, USA. In 2007-2008, he was a Visiting Professor at the University of California at San Diego, in 2014-2015 he was an Invited Professor at EPFL, Switzerland, and in 2021-2022 he was a Guest Professor at ETHZ. He is a co-author of the monographs "Interference in Large Wireless Networks" (NOW Publishers, 2009) and Stochastic Geometry Analysis of Cellular Networks (Cambridge University Press, 2018) and the author of the textbook "Stochastic Geometry for Wireless Networks" (Cambridge, 2012) and the blog stogblog.net. His scientific interests lie in networking and wireless communications, with an emphasis on cellular, amorphous, ad hoc (including D2D and M2M), cognitive, vehicular, and wirelessly powered networks. He served as an Associate Editor for the Elsevier Journal of Ad Hoc Networks, the IEEE Transactions on Mobile Computing (TMC), the ACM Transactions on Sensor Networks, as a Guest Editor for the IEEE Journal on Selected Areas in Communications, the IEEE Transactions on Vehicular Technology, and the EURASIP Journal on Wireless Communications and Networking, as a Steering Committee member of the TMC, and as the Chair of the Executive Editorial Committee of the IEEE Transactions on Wireless Communications (TWC). From 2017 to 2018, he was the Editor-in-Chief of the TWC. For both his M.Sc. and Ph.D. theses, he was awarded the ETH medal. He also received a CAREER award from the U.S. National Science Foundation in 2005 and three paper awards from the IEEE Communications Society, the 2010 Best Tutorial Paper award, the 2017 Stephen O. Rice Prize paper award, and the 2017 Best Survey paper award, and he is a Clarivate Analytics Highly Cited Researcher.

Risto Wichman received his M.Sc. and D.Sc. (Tech) degrees in electrical engineering from Tampere University of Technology, Finland, in 1990 and 1995, respectively. From 1995 to 2001, he worked at Nokia Research Center as a senior research engineer. In 2002, he joined the Department of Information and Communications Engineering, Aalto University School of Electrical Engineering, Finland, where he has been a full professor since 2008. His research interests lie in the physical layer of wireless communication systems, specifically in signal processing and communication theory.